PREDICTIVE MODELS FOR FORMATION RESISTIVITY FACTOR AND RESISTIVITY INDEX AT SUBSURFACE TEMPERATURES

Reza Askarinezhad[1*], *Meysam* Nourani[2]

[1]NORCE Norwegian Research Centre AS, Stavanger, Norway

[2]Stratum Reservoir AS, Stavanger, Norway

Abstract. This theoretical-experimental study focuses on the development of analytical models for predicting key petrophysical parameters such as the Formation Resistivity Factor (FRF), Resistivity Index (RI), and Apparent FRF in subsurface conditions characterized by varying temperatures. For this purpose, alongside the well-known Archie's equation, novel parameters including the thermal water resistivity modulus (WRM_T), thermal rock resistivity modulus (RRM_T), and thermal true resistivity modulus (TRM_T) were introduced. In the present study, a new approach is introduced based on a previous work by Nourani et al. (2023), which used similar concepts to assess the resistivity and overburden pressure. In accordance with the analytical models developed, it is evident that the FRF varies with temperature along with factors such as the FRF measured at a base temperature, which is typically considered ambient temperature, cementation factor, the coefficients of thermal expansions of pore and bulk volumes, and temperature difference. In addition, the proposed theoretical analyses shed light on the prediction of RI at desired temperatures based on RI data at ambient conditions together with parameters such as saturation exponent, pore and water thermal expansion coefficients, and temperature difference. Real core data derived from existing literature was used to validate the newly formulated FRF and RI models, which demonstrated their robustness to predict these parameters across a wide range of temperatures. The use of these models can be particularly beneficial for cases where it is impractical, inefficient, or unfeasible to carry out actual FRF and RI measurements at elevated hydrocarbon reservoir temperatures. A comprehensive framework can be used for predicting FRF and RI by incorporating these temperature-dependent models with those introduced by Nourani et al. (2023) for predicting FRF and RI under overburden pressure conditions at both realistic subsurface temperature and pressure conditions.

Introduction

Among the most essential petrophysical properties for log calibration and reservoir characterisation is the Archie's Resistivity Factor (PRF) and Resistivity Index (RI). Archie's empirical equations delineate the electrical characteristics of sandstones. These equations are formulated under the presumption that the sandstone is devoid of clay and exhibits strong water-wetting properties. Furthermore, they assume a straightforward, single-peaked pore structure, non-conductive rock grains, and that all water within the pores participates in electrical conduction [1–3].

Determining the volume of hydrocarbon initially in place (HCIIP) under reservoir conditions stands as a pivotal task in reservoir management. This calculation hinges upon factors such as water saturation, porosity, and the overall reservoir volume. Initially, the water saturation and porosity of the reservoir must be assessed. Subsequently, HCIIP can be determined by multiplying the product of one minus water saturation, porosity, and the total reservoir volume [4,5].

In order to accurately compute water saturation using Archie's equation, it becomes imperative to undertake the calibration of electrical logs. Within laboratory settings, FRF and RI experiments are meticulously designed to replicate reservoir conditions as closely as feasible. However, despite the meticulous efforts invested, these experiments often operate under conditions of lower overburden pressure and temperature compared to actual reservoir environments. Given the constraints of time, the complexity involved in measurements, and the higher expenses associated with conducting experiments at full reservoir conditions, practical considerations often necessitate adjustments. Thus, while striving for accuracy in simulating reservoir conditions, pragmatic approaches are adopted to balance the demands of scientific precision with practical limitations [6,7].

Hence, the testing conditions typically diverge from those encountered within the reservoir. Although the outcomes may not perfectly mirror real-world scenarios and may lack complete representativeness, they still offer valuable insights for petrophysical interpretations. Thus, it remains crucial to acknowledge and account for the inherent limitations of the testing conditions when

* Corresponding author: reas@norceresearch.no

scrutinizing the findings yielded by FRF tests. Nourani et al.[7] have formulated mathematical models utilizing Archie's equation to forecast FRF and RI across varying overburden pressures. The FRF models encompass two variations: the Single-FRF model and the Multi-FRF model. The Single-FRF model establishes a connection between the cementation exponent (m), pore volume compressibility (C_p[bar^{-1}]), bulk compressibility (C_b[bar^{-1}]), and the reference FRF through the following equation:

$$FRF_{P_2} = FRF_{P_1} e^{m\,(C_p - C_b)\Delta P} \quad (1)$$

The Multi-FRF model delineates the correlation between the rock resistivity modulus (RRM, represented by γ_{R_o}[bar^{-1}]), the difference in confining pressure (ΔP [bar]), and the reference FRF according to the following equation:

$$FRF_{P_2} = FRF_{P_1} e^{-\gamma_{R_{oP}}\Delta P} \quad (2)$$

The RI model's dependency lies in the saturation exponent (n), C_p, formation brine compressibility (C_{fbP}[bar^{-1}]), and the reference RI, expressed as follows:

$$RI_{P_2} = RI_{P_1} e^{n(C_{fbP} - C_p)\Delta P} \quad (3)$$

While the impact of overburden pressure on FRF and RI has been studied through modelling, there remains a notable lack of mathematical models capable of accurately balancing the results of experiments gauging FRF and RI under ambient temperature to accurately reflect reservoir conditions. This analytical-experimental investigation aims to investigate the interplay among FRF, RI, and subsurface temperature. The overarching goal is to devise mathematical models capable of forecasting FRF and RI across varying subsurface temperature conditions. Moreover, by integrating these temperature-dependent models with those proposed by Nourani et al. (2023) for predicting FRF and RI under different overburden pressure conditions, a comprehensive framework can be established for enhanced prediction of FRF and RI.

Development of the Thermal Models

Porosity denotes the proportion of voids or pores within a material, serving as a gauge for the available space. Typically, it is represented as the ratio of pore space volume (V_p) to the total bulk volume (V_b) of the rock. FRF quantifies the relationship between the resistivity of fully saturated rock with brine (R_o [Ωm]) and the resistivity of formation water (R_w [Ωm]). The calculation of FRF involves the interplay of porosity (φ [fraction]) and the cementation exponent, as expressed by the Archie equation[3]:

$$FRF = \frac{R_o}{R_w} = \varphi^{-m} \quad (4)$$

Resistivity Index (RI) stands as another critical dimensionless parameter. It is computed as the ratio of the rock's resistivity under partial water saturation (R_t [Ω m]) to its resistivity when fully saturated with water (R_o). This index reflects the amount of water present in the pore space, playing a pivotal role in the computation of the rock's electrical properties. Notably, RI correlates with water saturation (S_w [fraction]), as outlined in [1]:

$$RI = \frac{R_t}{R_o} = S_w^{-n} \quad (5)$$

Nourani et al.[7] introduced water resistivity modulus (WRM, $\gamma_{R_{wP}}$[bar^{-1}]), rock resistivity modulus (RRM,$\gamma_{R_{oP}}$[bar^{-1}]), and true resistivity modulus (TRM, $\gamma_{R_{tP}}$[bar^{-1}]) as indicators of the relative change in water resistivity, the resistivity of rock when fully saturated with brine, and the rock's resistivity under partial water saturation, respectively, in response to a pressure change, as delineated below [7]:

$$\gamma_{R_{wP}} = -\frac{1}{R_w}\frac{\partial R_w}{\partial P} \quad (6)$$

$$\gamma_{R_{oP}} = -\frac{1}{R_o}\frac{\partial R_o}{\partial P} \quad (7)$$

$$\gamma_{R_{tP}} = -\frac{1}{R_t}\frac{\partial R_t}{\partial P} \quad (8)$$

Now in this study analogous parameters known as the thermal water resistivity modulus (WRM$_T$, $\gamma_{R_{wT}}$[°C^{-1}]), thermal rock resistivity modulus (RRM$_T$, $\gamma_{R_{oT}}$[°C^{-1}]), and thermal true resistivity modulus (TRM$_T$, $\gamma_{R_{tT}}$[°C^{-1}]) are introduced. They differ from their counterparts by serving as indicators of the proportional shift in water resistivity, the resistivity of rock under complete brine saturation, and the rock's resistivity under partial water saturation, respectively, in reaction to temperature variations, as follows:

$$\gamma_{R_{wT}} = -\frac{1}{R_w}\frac{\partial R_w}{\partial T} \quad (9)$$

$$\gamma_{R_{oT}} = -\frac{1}{R_o}\frac{\partial R_o}{\partial T} \quad (10)$$

$$\gamma_{R_{tT}} = -\frac{1}{R_t}\frac{\partial R_t}{\partial T} \quad (11)$$

With the decrease of R_w, R_o and R_t with temperature, the gradients in Equations (9), (10) and (11) become negative numbers. Thus, the values of $\gamma_{R_{wT}}$, $\gamma_{R_{oT}}$, and $\gamma_{R_{tT}}$ are positive.

Development of the Thermal Water Resistivity Model

As a result of separating the R_w in Equation (9) and integrating, the R_w at a given temperature can be found as follows:

$$R_{wT_2} = R_{wT_1} e^{-\int_{T_1}^{T_2} \gamma_{R_{wT}} \partial T} \quad (12)$$

where R_{wT_1} is water resistivity at initial temperature. For small values of term ($\int_{T_1}^{T_2} \gamma_{R_{wT}} \partial T$), Equation (13) can be used to convert the exponential term in Equation (12) into a linear function[8].

$$e^{-\int_{T_1}^{T_2} \gamma_{R_{wT}} \partial T} \approx 1 - \int_{T_1}^{T_2} \gamma_{R_{wT}} \partial T \quad (13)$$

This approximation arises from the Maclaurin series expansion of e^{x}, where the term ($\int_{T_1}^{T_2} \gamma_{R_{wT}} \partial T$) was substituted for x and only the first two terms of the expansion were considered.
The Arp's formula, a well-established equation with a long history, can be used to determine how temperature affects water resistivity as follows [9]:

$$R_{wT_2} = R_{wT_1} \left(\frac{T_1+21.5}{T_2+21.5}\right) \quad (14)$$

Although this formula has been around for a long time, it remains one of the most widely embraced equations in the field, retaining its validity and continued use for estimating temperature-water resistivity relationships despite its advancing age [10,11].
Combining Equations (12), (13) and (14), the term ($\int_{T_1}^{T_2} \gamma_{R_{wT}} \partial T$) can be calculated as follows:

$$\int_{T_1}^{T_2} \gamma_{R_{wT}} \partial T = \frac{\Delta T}{T_2+21.5} \quad (15)$$

By substituting Equation (15) into Equation (12), one can estimate the impact of temperature on water resistivity as follows:

$$R_{wT_2} = R_{wT_1} e^{-\left(\frac{\Delta T}{T_2+21.5}\right)} \quad (16)$$

Equation (16) represents a refined adaptation of Arp's equation, particularly effective when temperature changes remain within a range of up to 10°C or less.

Development of the Thermal FRF Model

The R_o at a given temperature can be determined by separating the R_o in Equation (10) and integrating as follows:

$$R_{oT_2} = R_{oT_1} e^{-\int_{T_1}^{T_2} \gamma_{R_{oT}} \partial T} \quad (17)$$

where R_{oT_1} is rock resistivity at initial temperature. Combining Equations (4) and (10), yields the following equation:

$$\gamma_{R_{oT}} = -\frac{\varphi^m}{R_w} \frac{\partial \left(\frac{R_w}{\varphi^m}\right)}{\partial T} \quad (18)$$

The cementation factor and saturation exponent are expected to change due to changes in temperature, but for the sake of simplicity of deriving the mathematical models, it was assumed that m and n do not vary with temperature. Therefore, based on this assumption (i.e constant cementation exponent over the temperature interval of interest), taking the derivative of the term ($\frac{R_w}{\varphi^m}$) with respect to temperature in Equation (18) and rearranging it, the $\gamma_{R_{oT}}$ can be calculated using the following formula:

$$\gamma_{R_{oT}} = -\frac{1}{R_w}\frac{\partial R_w}{\partial T} + m\frac{1}{\varphi}\frac{\partial \varphi}{\partial T} \quad (19)$$

$\frac{\partial \varphi}{\partial T}$ represents the variation of porosity (V_p/V_b) with temperature. In order to find an analytical representation of this term, two new definitions are introduced. By definition, variations in the pore volume and bulk volume of a porous rock with temperature are presented by two terms of pore volume thermal expansion coefficient (C_{pT}) and bulk volume thermal expansion coefficient (C_{bT}), respectively, expressed in Equations (20) and (21):

$$C_{pT} = \frac{1}{V_p}\frac{\partial V_p}{\partial T} \quad (20)$$

$$C_{bT} = \frac{1}{V_b}\frac{\partial V_b}{\partial T} \quad (21)$$

Taking the derivative of the porosity with respect to temperature and replacing C_{pT} and C_{bT} from Equations (20) and (21) into it, yields the following equation:

$$\frac{\partial \varphi}{\partial T} = \varphi\,(C_{pT} - C_{bT}) \quad (22)$$

Equations (9), (19) and (22) can be combined to yield the following equation:

$$\gamma_{R_{oT}} = \gamma_{R_{wT}} + m\,(C_{pT} - C_{bT}) \quad (23)$$

As a result of replacing $\gamma_{R_{oT}}$ in Equation (17) with Equation (23), the following equation results:

$$R_{oT_2} = R_{oT_1} e^{-\int_{T_1}^{T_2} \gamma_{R_{wT}} \partial T + \int_{T_1}^{T_2} m(C_{bT} - C_{pT})\, \partial T} \quad (24)$$

As a result of dividing both sides of Equation (24) by Equation (12), the FRF at elevated temperatures can be calculated as follows:

$$FRF_{T_2} = FRF_{T_1} e^{\int_{T_1}^{T_2} m(C_{bT} - C_{pT})\, \partial T} \quad (25)$$

Consequently, by assuming constant pore and bulk volume thermal expansion coefficients over the temperature interval of interest, and calculating the integration in Equation (25), FRF_{T_2} can be determined using the following formula:

$$FRF_{T_2} = FRF_{T_1} e^{m\,(C_{bT} - C_{pT})\,\Delta T} \quad (26)$$

Development of the Thermal Apparent FRF Model

The reciprocal of electrical resistivity is referred to as conductivity. A rock's clay minerals act as separate conductors. As a result of the type, quantity, structure, and

distribution of clay in the rock, the effect of clay on the conductivity of the rock varies [12]. Waxman and Smits' equation relates the C_o to the C_w as follows[13]

$$C_o = \frac{C_w}{F^*} + \frac{BQ_v}{F^*} \quad (27)$$

where C_o [$\Omega^{-1}m^{-1}$], C_w [$\Omega^{-1}m^{-1}$], F^*, Q_v [meq/ml] and B [$(\Omega^{-1}m^{-1})/(meq/ml)$] are the brine-saturated rock conductivity, the brine conductivity, the shaly-sand FRF (apparent FRF), the equivalent conductance of sodium clay exchange cations and the volume concentration of sodium exchange cations associated with the clay, respectively.

Equation (28) demonstrates a linear relationship between C_w and C_o, simplifying the form of Equation (27) to:

$$C_o = aC_w + \mathrm{b} \quad (28)$$

where a is the slope ($\frac{1}{F^*}$), and b is the intercept ($\frac{BQ_v}{F^*}$). Therefore, the shaly-sand FRF can be calculated from the reciprocal of gradient ($\frac{1}{a}$) of the plot C_o as a function of C_w as [13,14]:

$$F^* = \frac{dC_w}{dC_o} \quad (29)$$

The following equation is obtained by taking the derivative of Equation (29) with respect to temperature:

$$\frac{\partial F^*}{\partial T} = \frac{1}{dC_o}\frac{\partial (dC_w)}{\partial T} - \frac{1}{dC_o}\frac{\partial (dC_o)}{\partial T}\frac{dC_w}{dC_o} \quad (30)$$

It is possible to define thermal water conductivity modulus (WCM_T) and thermal rock conductivity modulus (RCM_T) as follows:

$$\gamma_{C_{wT}} = -\frac{1}{dC_w}\frac{\partial (dC_w)}{\partial T} \quad (31)$$

$$\gamma_{C_{oT}} = -\frac{1}{dC_o}\frac{\partial (dC_o)}{\partial T} \quad (32)$$

A combination of equations (30), (31), and (32) gives the following equation:

$$\frac{\partial F^*}{\partial T} = F^*(\gamma_{C_{oT}} - \gamma_{C_{wT}}) \quad (33)$$

By integrating Equation (33) with respect to temperature, the apparent FRF at elevated temperatures can be calculated as follows:

$$F^*_2 = F^*_1 e^{\int_{T_1}^{T_2} (\gamma_{C_{oT}} - \gamma_{C_{wT}})\partial T} \quad (34)$$

In light of the fact that water conductivity approaches zero when salt concentration approaches zero, Equation (31) can be expressed as follows:

$$\gamma_{C_{wT}} = -\frac{1}{C_w}\frac{\partial C_w}{\partial T} \quad (35)$$

By substituting the water resistivity ($C_w = \frac{1}{R_w}$) in Equation (35) and taking its derivative with respect to temperature, combined with Equation (9), yields $\gamma_{C_{wT}} = -\gamma_{R_{wT}}$. It was demonstrated that the intercept of the line ($\frac{BQ_v}{F^*}$) in Equation (28) remains constant despite variations in temperature [15]. By assuming that the derivative of the intercept with respect to temperature is zero, and combining Equations (10), (28), and (32), we arrive at the following equation:

$$\gamma_{C_{oT}} = -\frac{1}{1-bR_o}\gamma_{R_{oT}} \quad (36)$$

Combining Equations (15), (23), (34), (35), and (36) results in the following:

$$F^*_{T_2} = F^*_{T_1} e^{K\Delta T} \quad (37)$$

where K is defined as follows:

$$K = \frac{(\frac{b}{C_o} - m(C_{bT} - C_{pT})(T_2 + 21.5))}{(T_2 + 21.5)(\frac{b}{C_o} - 1)} \quad (38)$$

As the fraction $\frac{b}{C_o}$ in Equation (38), is less than one, the denominator of Equation (38) is always negative. In order for K to be positive, the numerator of the fraction must also be negative.

Since the maximum value of $\frac{b}{C_o}$ approaches one, if the product of terms $(m(C_{bT} - C_{pT})(T + 21.5))$ exceeds one, the apparent FRF in Equation (37) will inevitably increase with increasing temperature.

$$m(C_{bT} - C_{pT})(T_2 + 21.5) > 1 \quad (39)$$

In clean sands, the excess conductivity (b) is zero. Consequently, Equation (37) simplifies to Equation (26).

Development of the Thermal RI Model

The calculation of RI can also be conducted using a similar modelling approach. From Equation (40) we can obtain R_t at elevated temperatures if R_t is separated in Equation (11) and integrated:

$$R_{tT_2} = R_{tT_1} e^{-\int_{T_1}^{T_2} \gamma_{R_{tT}}\partial T} \quad (40)$$

By dividing Equation (40) by Equation (17), the RI at a given temperature can be calculated as follows:

$$RI_{T_2} = RI_{T_1} e^{\int_{T_1}^{T_2} \gamma_{R_{oT}}\partial T - \int_{T_1}^{T_2} \gamma_{R_{tT}}\partial T} \quad (41)$$

Combining Equations (4), (5), and (8) results in the following equation:

$$\gamma_{R_{tT}} = -\frac{\varphi^m S_w{}^n}{R_w} \times \frac{\partial (\frac{R_w}{\varphi^m S_w{}^n})}{\partial T} \quad (42)$$

Consequently, by assuming constant cementation and saturation exponents over the temperature interval of interest and taking the derivative of the term $(\frac{R_w}{\varphi^m S_w{}^n})$ with respect to temperature in Equation (42) and rearranging it, the $\gamma_{R_{tT}}$ can be determined as follows:

$$\gamma_{R_{tT}} = -\frac{1}{R_w}\frac{\partial R_w}{\partial T} + m\frac{1}{\varphi}\frac{\partial \varphi}{\partial T} + n\frac{1}{S_w}\frac{\partial S_w}{\partial T} \quad (43)$$

Moreover, the thermal expansion of formation brine; C_{fbT}, is expressed as follows:

$$C_{fbT} = \frac{1}{V_w}\frac{\partial V_w}{\partial T} \quad (44)$$

where V_w is the volume of the formation brine; this volume can be estimated through Equation (45):

$$V_w = \varphi V_b S_w \quad (45)$$

Combining Equations (43) and (44) and taking the derivative of the term $(\varphi V_b S_w)$ with respect to temperature and replacing C_{pT} and C_{bT} from Equations (20) and (21) into it, yields the following equation:

$$\frac{1}{S_w}\frac{\partial S_w}{\partial T} = C_{fbT} - C_{pT} \quad (46)$$

Thus, the $\gamma_{R_{tT}}$ can be calculated by replacing Equations (9), (22) and (46) into Equation (43) as below:

$$\gamma_{R_{tT}} = \gamma_{R_{wT}} + m\left(C_{pT} - C_{bT}\right) + n\left(C_{fbT} - C_{pT}\right) \quad (47)$$

By replacing the $\gamma_{R_{oT}}$ and $\gamma_{R_{tT}}$ (from Equations (23) and (47) respectively) in Equation (41), the RI at elevated temperature can be calculated as follows:

$$RI_{T_2} = RI_{T_1} e^{\int_{T_1}^{T_2} [n(C_{Tp} - C_{fbT})]\partial T} \quad (48)$$

Consequently, by assuming constant saturation exponent and thermal expansion of formation brine over the temperature interval of interest, and calculating the integration in Equation (48), RI_{T_2} can be calculated using the following formula:

$$RI_{T_2} = RI_{T_1} e^{n(C_{pT} - C_{fbT})\Delta T} \quad (49)$$

From integration of Equation (46) with respect to temperature, the S_w at a given temperature can be estimated as follows:

$$S_{wT_2} = S_{wT_1} e^{(C_{fbT} - C_{pT})\,\Delta T} \quad (50)$$

Moreover, Nourani et al [7] calculated S_w at a given overburden pressure using the following formula:

$$S_{wP_2} = S_{wP_1} e^{(C_p - C_{fbP})\,\Delta P} \quad (51)$$

Combining the Barometric and the Thermal Models

The literature indicates that the electrical properties of the sandstones under study are affected by both overburden pressure and temperature. Previous research has shown that the combined effect of these factors on the sandstones' electrical properties is approximately equivalent to the sum of their individual effects, as reported by various researchers [16,17]. This suggests that while overburden pressure and temperature each have distinct impacts on the sandstones' electrical behaviour, their combined influence follows an additive trend [16,17]. Therefore, it has been assumed that predicting FRF and RI under specific overburden pressures and temperatures requires a systematic approach involving two distinct steps as shown in Figure 1. First, a constant temperature is maintained at ambient temperatures while the overburden pressure is manipulated. Step Two involves increasing the temperature of the sample while maintaining a constant overburden pressure equivalent to Step One.

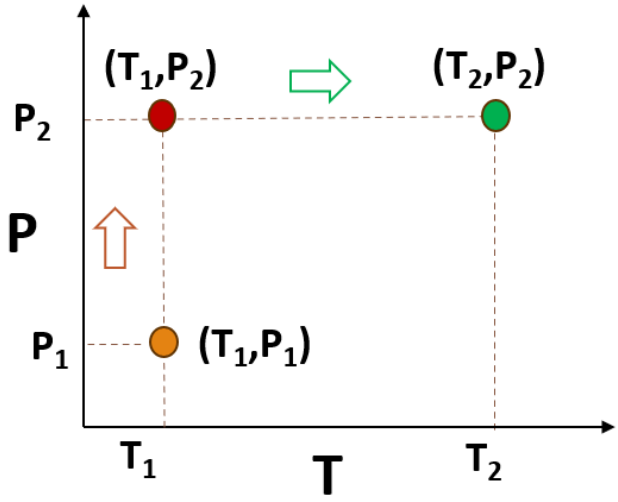

Fig. 1. Two-step process for estimating the FRF and RI at specific overburden pressure and temperature conditions have been assumed. Step One involves manipulating overburden pressure while maintaining constant temperature, followed by Step Two where the sample undergoes controlled temperature increase while keeping overburden pressure constant.

First, the FRF and RI are predicted at the given overburden pressure and constant temperature using Equations (1) and (3) as follows:

$$FRF_{T_1,P_2} = FRF_{T_1,P_1} e^{m\,(C_p - C_b)\Delta P} \quad (52)$$

$$RI_{T_1,P_2} = RI_{T_1,P_1} e^{n(C_{fbP} - C_p)\Delta P} \quad (53)$$

Next, the FRF and RI are predicted at the elevated temperature and constant overburden pressure by inserting FRF_{T_1,P_2} and RI_{T_1,P_2} from Equations (52) and (53) into Equations (26) and (49), respectively. Accordingly, Equations (54) and (55) predict the FRF and RI at the specified overburden pressure and temperature.

$$FRF_{T_2,P_2} = FRF_{T_1,P_1}\, e^{m\,[(C_p - C_b)\Delta P + (C_{bT} - C_{pT})\,\Delta T]} \quad (54)$$

$$RI_{T_2,P_2} = RI_{T_1,P_1}\; e^{\,n[(C_{fbP} - C_p)\Delta P + (C_{pT} - C_{fbT})\,\Delta T]} \quad (55)$$

Furthermore, it is also possible to estimate the saturation of water at the specified overburden pressure and temperature by combining Equations (50) and (51), as follows:

$$S_{wT_2,P_2} = S_{wT_1,P_1}\; e^{\,[(C_p - C_{fbP})\Delta P + (C_{fbT} - C_{pT})\,\Delta T]} \quad (56)$$

Results and Discussion

In a semilogarithmic plot passing through $\Delta T = 0$, with $FRF_{T_2} = FRF_{T_1}$, $\frac{FRF_2}{FRF_1}$ versus temperature difference leads to a straight line with slope $m\,(C_{bT} - C_{pT})$:

$$m\,(C_{bT} - C_{pT}) = \frac{Ln\frac{FRF_2}{FRF_1}}{\Delta T} \quad (57)$$

Using Equation (26), FRF can be predicted at any elevated temperature using the obtained term ($m\,(C_{bT} - C_{pT})$). Figure 2 shows the Ln $\frac{\mathrm{FRF_2}}{\mathrm{FRF_1}}$ versus the temperature difference for four sandstone samples. The dataset has been extracted from published literature [18]. In Table 1, the term ($m\,(C_{bT} - C_{pT})$) were calculated based on the slopes of the lines in Figure 2.

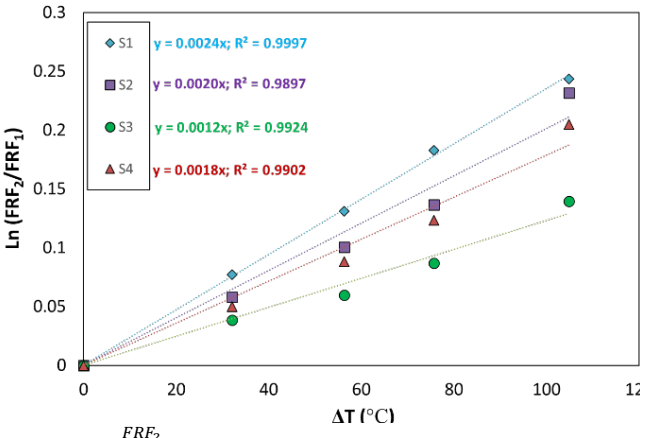

Fig. 2. Ln $\frac{FRF_2}{FRF_1}$ versus temperature difference. According to Equation (57), the term ($m\,(C_{bT} - C_{pT})$) were calculated by the slope of lines for four sandstone samples from literature [18].

Table 1. The calculated term ($m\,(C_{bT} - C_{pT})$) from the slope of the lines in Figure 2.

Sample	$m\,(C_{bT} - C_{pT})$ (°C^{-1})	R^2
S1	2.35×10^{-3}	0.9997
S2	2.01×10^{-3}	0.9897
S3	1.23×10^{-3}	0.9924
S4	1.79×10^{-3}	0.9992

Figure 3 illustrates the modelled FRF at elevated temperatures based on the values from Table 1. The FRF predicted by the model and the experimental data measured in the laboratory are very well matched.

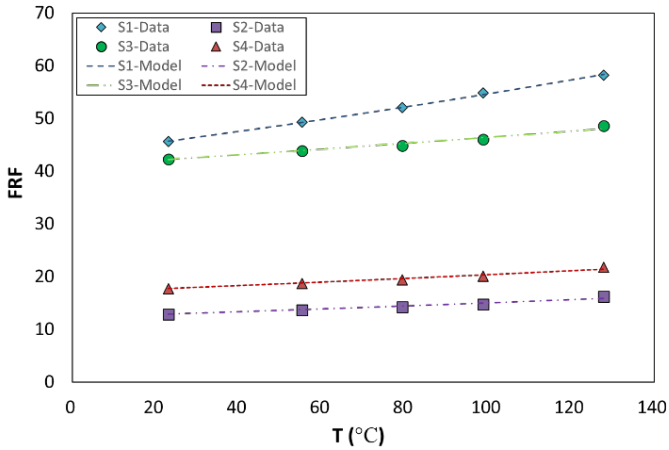

Fig. 3. Measured and calculated FRF at elevated temperatures for six sandstone samples [18].

The FRF increases as the temperature increases as predicted by Equation (26), which is in agreement with experimental results in the literature [15,17,19,20].
Using a similar approach for overburden pressure, in a semilogarithmic plot passing through $\Delta P = 0$, with $FRF_{P_2} = FRF_{P_1}$, $\frac{FRF_2}{FRF_1}$ versus overburden pressure leads to a straight line with slope $m\,(C_p - C_b)$:

$$m\,(C_p - C_b) = \frac{Ln\frac{FRF_2}{FRF_1}}{\Delta P} \quad (58)$$

Equation (1) can be used to predict FRF at any overburden pressure using the obtained term ($m\,(C_p - C_b)$). In Figure 4, the Ln $\frac{\mathrm{FRF_2}}{\mathrm{FRF_1}}$ versus the overburden pressure difference is illustrated for four samples of sandstone. Data have been derived from published literature [18]. Based on the slopes of the lines in Figure 4, the term ($m\,(C_p - C_b)$) was calculated in Table 2.

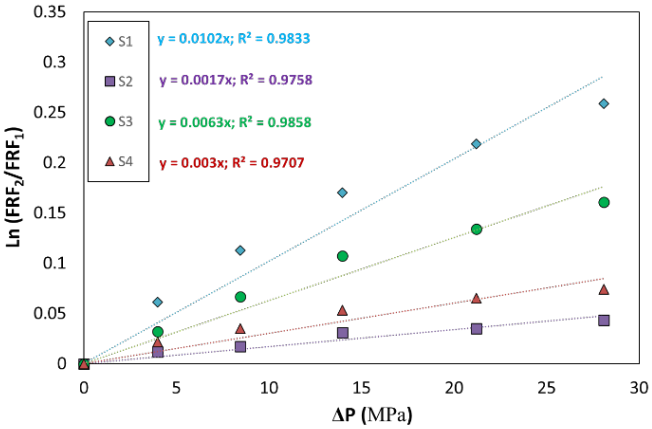

Fig. 4. Ln $\frac{FRF_2}{FRF_1}$ versus overburden pressure difference. According to Equation (58), the term ($m\,(C_p - C_b)$) were calculated by the slope of lines for four sandstone samples from literature [18].

Table 2. The calculated term ($m\ (C_p - C_b)$) from the slope of the lines in Figure 4.

Sample	$m\ (C_p - C_b)$ (MPa $^{-1}$)	R^2
S1	10.20×10^{-3}	0.9833
S2	1.70×10^{-3}	0.9758
S3	6.27×10^{-3}	0.9858
S4	3.02×10^{-3}	0.9707

Based on the values presented in Table 2, Figure 5 illustrates the modelled FRF under overburden pressure. Model predictions and experimental measurements are very closely matched.

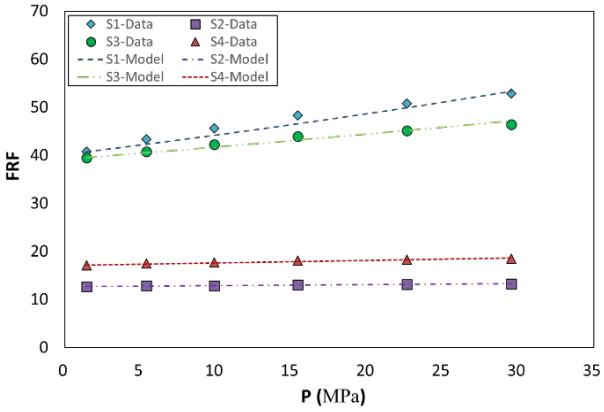

Fig. 5. Measured and calculated overburden FRF for six sandstone samples [18].

For the purpose of illustrating the application of the developed combined FRF model, we assume that the value of FRF at 20 MPa and 100°C is desired for samples S1 through S4. FRF has been measured at 23.1°C and 1.44 MPa at the initial temperature and overburden pressure in Figures 3 and 5 [18]. Therefore, the difference in temperature and overburden pressure is 76.90°C and 18.56 MPa, respectively. The FRF was calculated in Table 3 based on measured FRF at base temperature and overburden pressure, ΔP and ΔT, the coefficients obtained in Tables 1 and 2, and using Equation (54).

Table 3. The estimated FRF at 20 MPa and 100°C using Equation (54) and the obtained coefficients in Tables 1 and 2.

Sample	FRF_{T_1,P_1}	$FRF@\ 20\ MPa\ \&\ 100°C$
S1	40.75	58.99
S2	12.64	15.23
S3	39.50	48.78
S4	17.12	20.77

An understanding of the exact values of thermal expansion coefficients for bulk, thermal expansion coefficients for pores, as well as volume compressibility coefficients for bulk and volume compressibility coefficients for pores is valuable. Nevertheless, it is not necessary to know these values in order to calculate the product of cementation factor times the difference between pore and bulk volume compressibility coefficients, as well as the product of cementation factor times the difference between bulk and pore volume thermal expansions, which are necessary for the prediction of FRF by Equation (54). By measuring FRF under three different conditions (T_1, P_1), (T_1, P_2), and (T_2, P_2), one can obtain the parameters necessary to make the integrated FRF model operational. Additionally, the three FRF measurements are the same measurements that are usually conducted in the SCAL program when measuring capillary pressure by the Porous Plate method (PcRI test). In a PcRI test, FRF is typically measured at ambient temperature and 20 bar (T_1, P_1), then at ambient temperature and reservoir overburden pressure (T_1, P_2). In addition, the R_t is obtained at reservoir pressure and temperature. When the sample is saturated with brine, the PcRI measurement begins and therefore the first R_t measurement equals the R_o measurement. Thus, FRF at reservoir temperatures and pressures is also commonly available (T_2, P_2). In consequence, no additional measurements are necessary in order to make the integrated FRF model operational.

Previous studies have yielded contradictory findings concerning the impact of temperature on the apparent FRF. While some researchers indicate an elevation in the apparent FRF with rising temperature [15,18,20,21], others [17,22–24] suggest a decrease. This inconsistency is primarily attributed to differences in the types of rock samples utilized and variations in their clay content [18]. The models developed in this study have the capability to provide explanations for both of these observed phenomena.

The equations (37) and (38) indicate that the apparent FRF can increase or decrease as the temperature increases, confirming the experimental data in the literature. The two situations can occur in reservoirs with normal temperatures (T<200°C). First, FRF increases with increasing temperature for samples with low excess conductivity, which indicates a low clay content in the reservoir. Second, FRF appears to decrease with increasing temperature for samples exhibiting high excess conductivity, suggesting that the reservoir contains a significant amount of clay.

In addition, for measurements conducted at temperatures above 400°C, which are more applicable to geothermal reservoirs, inequality (39) can be satisfied, and for that temperature range, the developed models predict an increase in apparent FRF with temperature. Consequently, the developed models provide comprehensive insights into the behavior of the apparent FRF under changing thermal conditions. This study reconciles the conflicting findings of previous studies to gain a more nuanced understanding of how temperature influences apparent FRF.

Figure 6 illustrates an example of predicting saturation exponents at 90°C for the data from literature [25]. Based on the saturation at 30°C, Equation (51) is used to estimate the saturation at 90°C. RI at 30°C at the calculated water saturation is then used in Equation (49) to calculate RI at 90°C. The predicted saturation exponent matches the actual value excellently with a precision of one decimal place.

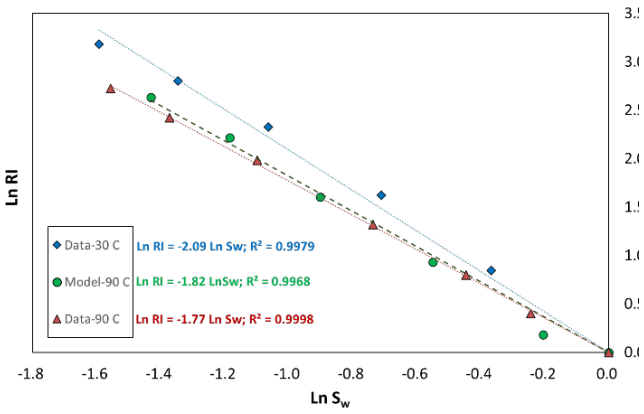

Fig. 6. Example, saturation exponent calculated at 90°C using Equations (49) and (51).

Conclusions

This work defines new electrical resistivity moduli to express the temperature-dependent dependencies on electrical properties, analogous to the electrical resistivity moduli defined by Nourani et al. [7] (to express the pressure dependency of electrical properties in rock/fluid systems). Using available ambient measurements, high-precision predictive tools have been developed to facilitate obtaining electrical properties at realistic reservoir conditions. Following is a summary of the main outcome of this study:

- Mathematical models have been developed for predicting FRF, RI, and apparent FRF at elevated temperatures in order to develop a prediction technique. There are several parameters included in the FRF Model, including the FRF at ambient or initial temperature, the cementation exponent, the thermal expansion coefficients for bulk and pores, as well as the temperature difference between the desired temperature and the ambient/initial temperature. The RI Model includes RI at ambient/initial temperature, the saturation exponent, the pore volume thermal expansion coefficient, thermal expansion of formation brine and temperature difference between the desired temperature and ambient/initial temperature.

- In order to verify the validity of the developed FRF models, their applications were conducted on actual core data obtained from existing literature. As a result of the validation, the FRF models were able to predict the behaviour of FRF for the investigated elevated temperature with less than 3% relative error.

- Through the integration of these temperature-dependent models with the ones introduced by Nourani et al. (2023) for predicting FRF and RI under overburden pressure conditions, a comprehensive framework for predicting FRF and RI was established. With this comprehensive approach, FRFs and RIs can be predicted for a wide range of reservoir conditions, including subsurface temperature and overburden pressure.

The authors extend their gratitude to NORCE Norwegian Research Centre AS and Stratum Reservoir AS for generously granting permission to publish this collaborative paper.

Nomenclature

a Slope of the line in Equation (28), dimensionless
b Intercept of the line in Equation (28), $\Omega^{-1}m^{-1}$
B Volume concentration of sodium exchange cations associated with the clay, $(\Omega^{-1}m^{-1})/(meq/ml)$
C_b Bulk compressibility, bar^{-1}/MPa^{-1}
C_{bT} Bulk volume thermal expansion coefficient, $°C^{-1}$
C_{fbP} Formation brine compressibility, bar^{-1}
C_{fbT} Thermal expansion of formation brine, $°C^{-1}$
C_o Brine-saturated rock conductivity, $\Omega^{-1}m^{-1}$
C_p Pore volume compressibility, bar^{-1}/MPa^{-1}
C_{pT} Pore volume thermal expansion coefficient, $°C^{-1}$
C_w Brine conductivity, $\Omega^{-1}m^{-1}$
ΔP Confining pressure difference, bar/MPa
ΔT Temperature difference, °C
φ Porosity, fraction
F^* Shaly-sand FRF (apparent FRF), dimensionless
FRF Formation Resistivity Factor, dimensionless
γ_{C_oT} Thermal rock conductivity modulus, $°C^{-1}$
γ_{C_wT} Thermal water conductivity modulus, $°C^{-1}$
γ_{R_oP} Rock resistivity modulus (RRM), bar^{-1}
γ_{R_oT} Thermal rock resistivity modulus (RRM_T), $°C^{-1}$
γ_{R_tP} True resistivity modulus (TRM), bar^{-1}
γ_{R_tT} Thermal true resistivity modulus (TRM_T), $°C^{-1}$
γ_{R_wP} Water resistivity modulus (WRM), bar^{-1}
γ_{R_wT} Thermal water resistivity modulus (WRM_T), $°C^{-1}$
$HCIIP$ Volume of hydrocarbon initially in place at reservoir conditions, m^3
m Cementation factor, dimensionless
n Saturation exponent, dimensionless
P Pressure, bar/MPa
Q_v Equivalent conductance of sodium clay exchange cations, meq/ml
RI Resistivity Index, dimensionless
R_o Resistivity of rock fully saturated w/brine, Ωm
R_t Resistivity of rock partially saturated w/brine, Ωm
R_w Formation water resistivity, Ωm
S_w Water saturation, fraction
T Temperature, °C
V Volume of the reservoir, m^3
V_b Bulk volume, m^3
V_p Pore space volume, m^3
V_w Volume of the formation brine, m^3

References

1. S.L. Carter, H.H. Power, Log Analyst **2** (1962).

2. N. Mungan, E.J. Moore, J. Can. Pet. Technol. **7**, 20-5 (1968).
3. G.E. Archie, Trans. AIME **146**, 54-62 (1942).
4. M. Fleury, M. Efnik, M.Z. Kalam, Proc. Int. Symp. Soc. Core Analysts, Abu Dhabi, UAE (2004) p. 5-9.
5. P. Masoudi, A. Zahedi, M. Ali, A. Farshid, Z. SeyedMohammad, Energy Explor. Exploit. **29**, 543-57 (2011).
6. C. McPhee, J. Reed, I. Zubizarreta, Core analysis: a best practice guide (Elsevier, 2015)
7. M. Nourani, S. Pruno, M. Ghasemi, M.M. Fazlija, B. Gonzalez, H.-E. Rodvelt, Petrophysics **64**, 353-66 (2023) https://doi.org/10.30632/PJV64N3-2023a3.
8. E. Kreyszig, Advanced Engineering Mathematics (John Wiley & Sons. INC, Singapore, 1993).
9. J.J. Arps, J. Pet. Technol. **5**, 17-20 (1953).
10. D. Kennedy, SPWLA Annu. Log. Symp. (2020) p. D013S002R002.
11. D. Tiab, E.C. Donaldson, Petrophysics: theory and practice of measuring reservoir rock and fluid transport properties (Gulf Professional Publishing, 2015).
12. O. Torsæter, M. Abtahi, Experimental reservoir engineering laboratory workbook (Norwegian University of Science and Technology, 2003).
13. M.H. Waxman, L.J.M. Smits, Soc. Pet. Eng. J. **8**, 107-22 (1968).
14. M.H. Waxman, E.C. Thomas, Electrical conductivities in shaly sands-I (n.d.) p. 213-25.
15. G.O. Brannan, W.D. Von Gonten, SPWLA Annu. Log. Symp. (1973) p. SPWLA-1973.
16. X.D. Jing, J.S. Archer, T.S. Daltaban, Mar. Pet. Geol. **9**, 115-27 (1992).
17. D.W. Hilchie, The effect of pressure and temperature on the resistivity of rocks (The University of Oklahoma, 1964).
18. X.D. Jing, J.S. Archer, T.S. Daltaban, Mar. Pet. Geol. **9**, 115-27 (1992).
19. K.H. Hashmy, J.M. Campbell, SPWLA 7th Annu. Log. Symp., OnePetro (1966).
20. S.S. Marsden, H.J. Ramey, S.K. Sanyal, Log Analyst **14** (1973).
21. D.P. Helander, The effect of pore configuration, pressure, and temperature on rock resistivity (The University of Oklahoma, 1965).
22. J.W. Kern, W.A. Hoyer, M.M. Spann, SPWLA Annu. Log. Symp. (1977) p. SPWLA-1977.
23. H. Ucok, Temperature Dependence of The Electrical Resistivity Of Aqueous Salt Solutions And Solution-Saturated Porous Rocks (1980).
24. E.I. Parkhomenko, Rev. Geophys. **20**, 193-218 (1982).
25. M.E.-A. Dolka, SPE Middle East Oil Gas Show Conf. (1981) p. SPE-9617.